Moisture Modes and the Madden-Julian Oscillation

David J. Raymond*

New Mexico Tech

Socorro, New Mexico, USA

and

Željka Fuchs

University of Split

Split, Croatia

November 18, 2008

---

*Corresponding author address: David J. Raymond, Physics Department, New Mexico Tech, 801 Leroy Place, Socorro, NM 87801. E-mail: raymond@kestrel.nmt.edu

Abstract

Moisture mode instability is thought to occur in the tropical oceanic atmosphere when precipitation is a strongly increasing function of saturation fraction (precipitable water divided by saturated precipitable water) and when convection acts to increase the saturation fraction. A highly simplified model of the interaction between convection and large-scale flows in the tropics suggests that there are two types of convectively coupled disturbances, the moisture mode instability described above and another unstable mode dependent on fluctuations in the convective inhibition. The latter is associated with rapidly moving disturbances such as the equatorially coupled Kelvin wave.

A toy aquaplanet beta-plane model with realistic sea surface temperatures produces a robust Madden-Julian oscillation-like disturbance which resembles the observed phenomenon in many ways. Convection in this model exhibits a strong dependence of precipitation on saturation fraction and does indeed act to increase this parameter in situations of weak environmental ventilation of disturbances, thus satisfying the criteria for moisture mode instability. In contrast, NCEP's closely related GFS and CFS models do not produce a realistic MJO. Investigation of moist entropy transport in NCEP's final analysis (FNL), the data assimilation system feeding the GFS, indicates that convection tends to decrease the saturation fraction in these models, precluding moisture mode instability in most circumstances. Thus, evidence from a variety of sources suggests that the MJO is driven at least in part by moisture mode instability.

1 Introduction

The Madden-Julian oscillation (MJO) is notoriously difficult for global models to simulate (Lin et al. 2006). Furthermore, there is no universally accepted theory of this phenomenon. Zhang (2005) describes the essential characteristics of the MJO in his comprehensive review. These can be summarized briefly as follows:

1. The MJO is a global-scale, convectively coupled, eastward-moving disturbance with roots in the tropics. The convective aspects are most obvious in the Indian and western Pacific oceans, with a small convectively coupled region in the far eastern Pacfic north of the equator in the boreal summer.

2. Eastward-moving variance has a broad range of periods extending over $30-100$ d. The broad convective envelope of the MJO moves eastward in the Indian and west Pacific oceans at about 5 m s^{-1}. Though the convective signal disappears outside of the regions noted above, a global, eastward-propagating signal exists in the zonal wind in the upper troposphere which moves much more rapidly through the non-convectively coupled longitudes.

3. Easterly wind anomalies exist in the lower troposphere to the east of the active convection and in the upper troposphere to the west, while westerly anomalies occur to west of the convection in the lower troposphere and to the east in the upper troposphere. Cyclonic wind anomalies occur on the north and south flanks of the convection in the lower troposphere, whereas anticyclonic anomalies occur in the upper troposphere. All of this is consistent with the Gill (1980) model for the response of the troposphere to near-equatorial heating.

4. At low levels the strongest winds in equatorial latitudes are westerlies, which tend to occur either concident with or to the west of the most intense convection. The former pattern tends to develop more in the western Pacific, while the latter is more prevalent

in the Indian Ocean.

5. Along the equator there is a westward tilt to the heating and vertical velocity pattern of the MJO in convectively coupled regions.

6. The large-scale convective envelope of the MJO contains a myriad of synoptic scale disturbances moving both to the east and west. These have been variously identified as equatorial Kelvin waves, mixed Rossby-gravity waves, inertio-gravity waves, easterly waves, tropical cyclones, and westerly wind bursts.

7. The MJO follows latitudinal excursions in the sea surface temperature (SST) maximum, with the strongest signals north and south of the equator lagging the respective solstices by about 2 mon. In between, the MJO tends to be somewhat weaker. Significant interactions exist between the MJO and the Asian monsoon.

Zhang (2005) describes the extensive history of theory and modeling aimed at understanding the MJO. In the interests of brevity this is not repeated here. Instead we focus on recent promising developments.

The treatment of convection in large-scale atmospheric models is without a doubt the most problematic aspect of simulations of the MJO (Slingo et al. 1996). There is still no reliable method for testing the performance of cumulus parameterizations. However, the evaluation of such parameterizations against cloud-resolving numerical models of convection (CRMs) has begun to change this situation. Derbyshire et al. (2004) showed using two different CRMs that deep convection is very sensitive to tropospheric relative humidity and that a number of widely used cumulus parameterizations did not reproduce this sensitivity. This behavior has been confirmed by other numerical models (Lucas et al. 2000; Tompkins 2001; Raymond and Zeng 2005) and in observations (Sherwood 1999; Bretherton et al. 2004; Back and Bretherton 2006). Raymond (2007) showed that tuning a cumulus parameterization to a CRM in the context of the weak temperature gradient approximation (Sobel and Bretherton 2000; Sobel et al. 2001; Mapes 2004; Raymond and Zeng 2005) results in

more rapidly developing zonal wind variance on intraseasonal time scales compared to the untuned version of Raymond (2001). The weak temperature gradient approximation when applied to a single column model approximates the effect of the tropical environment by forcing the column to maintain buoyancy equilibrium with its surroundings via an imposed vertical velocity profile which counters heating with diabatic cooling. This vertical velocity, along with the convergence and divergence it implies, also transports moisture.

Grabowski (2001, 2003) found that a large-scale model in which the cumulus parameterization is replaced by a small CRM in each grid box produces an MJO-like disturbance. The key element facilitating the production of this disturbance is the buildup of humidity in the convecting region. Such a "superparameterization" was also used by Khairoutdinov et al. (2005) in place of the standard Zhang-McFarlane (1995) parameterization in the National Center for Atmospheric Research's Community Atmosphere Model (CAM). Comparison with the standard CAM showed a much enhanced MJO. Plots of rainfall rate versus saturation fraction (precipitable water divided by saturated precipitable water) in these two simulations show much more realistic results in the version with the superparameterization than in the standard version (Zhu et al. 2008). The standard version exhibits too much rainfall at low saturation fractions and not enough at higher saturation fractions compared to Bretherton et al. (2004).

The gross moist stability (GMS; Neelin and Held 1987) is an important concept when dealing with the dynamics of convectively coupled systems. Roughly speaking, the GMS is proportional to the net export due to lateral flows through the sides of a dynamical system of some quantity which is conserved by moist processes. No such quantity is precisely conserved, but two of the most useful are the moist static energy and the moist entropy. The GMS is normalized by some quantity proportional to the amount of convection occurring in the system of interest. Various different normalizing quantities are used as well, such as the total mass flowing through the system or the amount of moisture extracted by the system from the flow.

Theoretical support exists for the idea that moisture anomalies constitute the dynamical backbone of stationary or slowly propagating convectively coupled modes in the tropics (Fuchs and Raymond 2002, 2005, 2007; Raymond and Fuchs 2007). Free-standing "moisture modes" in a homogeneous environment were found in these results to be unstable for a wide range of spatial scales if the GMS is negative. However, moisture modes can also exist with positive GMS when there is an independent forcing mechanism, e. g., advection across a moisture gradient in a rotating environment (Sobel et al. 2001) or self-enhanced surface heat fluxes and suppression of radiative losses, as in a tropical cyclone (Emanuel 1986; Raymond et al. 2007). The latter situation can be represented as an effective negative GMS (Su and Neelin 2002; Masahiro Sugiyama, personal communication 2008) in situations where the GMS as formally defined is positive.

The effects of negative GMS in a convectively coupled system have not been extensively considered. López-Carrillo and Raymond (2005) found from Doppler radar and sounding observations that the net moist entropy export by convective systems, and hence the GMS, could take on either positive or negative values in the equatorial western Pacific. The positive values were associated with mature mesoscale systems with a heavy stratiform component, while negative values were associated with more convective regimes and a vertical mass flux maximum located at lower levels. The saturation fraction tended to be larger for positive GMS cases.

Bretherton et al. (2005) found negative GMS in a large-domain CRM in which the convection underwent self-aggregation. Such concentration of convection into a limited region surrounded by dry air can be considered to be a case of moisture mode instability.

Negative GMS occurs when the outflow-weighted moist entropy is less than the inflow-weighted value of this variable. For a simple dipole structure with inflow at low levels and outflow at high levels, this can happen when the level of maximum vertical mass flux is lower than the minimum in the environmental moist entropy profile. This occurred in the results of López-Carrillo and Raymond (2005). However, the situation is more complex in

the numerical results of Bretherton et al. (2005); in this case low moist static energy air is exported from the simulated convection in a thin detrainment layer near the top of the boundary layer. Such detainment is often seen from deep convective regions in the tropics, as documented by Zhang et al. (2004). Raymond and Blyth (1986) observed such detrainment in continental convection and attributed it to buoyancy sorting following vertical mixing of air in convection. However, irrespective of how negative GMS is achieved, it results in convection moistening its own environment rather than drying it, as occurs when the GMS is positive. Sobel and Neelin (2006) found that negative GMS associated with boundary layer flows tends to produce more concentrated intertropical convergence zones in a global model of intermediate complexity.

The purpose of this paper is to present evidence that the MJO is a moisture mode which depends on the presence of negative GMS for its existence. To this end we first explore the sensitivity of the analytical model results of Raymond and Fuchs (2007) to both positive and negative GMS, showing that moisture modes only appear in this model with negative GMS, at least in the absence of additional forcing. Next we analyze results from a slightly enhanced version of the toy equatorial beta plane aquaplanet model of Raymond (2007) in which a strong, MJO-like disturbance develops. Finally, we examine the output of the National Oceanic and Atmospheric Administration's operational Final Analysis (FNL), which incorporates the same physics as their Global Forecast System (GFS) and the associated Climate Forecast System (CFS). The CFS, like many other global models, is known to produce a rather weak MJO (Jia-Lin Lin, personal communication 2008). The toy model exhibits negative GMS in the equatorial western Pacific whereas the FNL does not. These results together suggest that the MJO is in essence a moisture mode and that negative GMS is required for its existence.

2   Analytical model results

Raymond and Fuchs (2007) developed a two-dimensional, linearized model of convectively coupled disturbances in which convection is forced by a combination of the precipitable water anomaly and the relaxation of convective inhibition (CIN). Two types of unstable modes are found in this model, the convectively coupled gravity mode and the moisture mode, the latter of which is stationary (in the linearized limit) except in the presence of mean zonal surface winds. Long-wavelength moisture modes move in the direction opposite to the zonal wind as found by Emanuel (1987). The gravity modes move at the observed speeds of convectively coupled equatorial Kelvin waves and have the same zonal dynamics as such waves.

The gross moist stability in Raymond and Fuchs (2007) is defined

$$\Gamma_M = \int_0^h (\partial s/\partial z) w dz \bigg/ \int_0^h (\partial s_d/\partial z) w dz \qquad (1)$$

where h is the height of the tropopause, w is the vertical velocity, s is the moist entropy, and s_d is the dry entropy. This normalization is somewhat different from the gross moist stability of Neelin and Held (1987). Because of this, we refer to Γ_M as the *normalized gross moist stability* or the NGMS. The NGMS is adjusted in this model by varying the vertical profile of moist entropy, since the vertical velocity exhibits to a good approximation a fixed fundamental baroclinic mode sinusoidal dependence on height for all modes.

The dispersion relation for the linearized theory in Raymond and Fuchs (2007) includes the effects of non-zero NGMS. However, plots were only presented in that paper for zero NGMS. Figure 1 shows the dispersion relations for moisture modes occurring with various negative values of the NGMS, but no wind-induced heat exchange or cloud-radiation interactions. Note that instability is strongest at shorter wavelengths, decreasing somewhat at lower wavenumbers. This decrease is due primarily to the effects of CIN. Turning off CIN removes most of this decrease. Moisture modes are stable for positive NGMS. This follows from the instability mechanism for moisture modes; instability occurs when convection produces an

8

environment which is favorable for the production of more moisture mode convection, i. e., by increasing the saturation fraction. This occurs when the NGMS is negative.

Figure 2 shows the corresponding dispersion relation for convectively coupled gravity waves. This mode is only weakly sensitive to the NGMS, with positive NGMS values resulting in slightly increased instability. The instability of this mode depends primarily on the CIN term in the convective forcing, and the weak dependence on NGMS therefore makes sense.

For our purposes here, the important result from this model is that instability of the moisture mode depends on the existence of negative NGMS. Cloud-radiation interactions and wind-induced heat exchange (WISHE) are able to destabilize the moisture modes as well, but only by virtue of supplying moisture feedbacks similar to those supplied by negative NGMS.

3 The toy beta-plane model

3.1 Governing equations

The model used for this study is an improved version of that used by Raymond (2001, 2007). It is an equatorial beta-plane channel model with the novel vertical coordinate

$$\sigma = \frac{\theta - \theta_B}{\theta_T - \theta_B} \tag{2}$$

where θ is the potential temperature and θ_B and θ_T are the potential temperatures at the surface and domain top. θ_T is held constant and is also assumed to be a constant pressure surface, while θ_B is in general a function of position and time. The constant pressure upper boundary condition is reflective, so a sponge layer is placed in the upper part of the domain. The governing equations for this model are as follows.

Mass:

$$\frac{\partial \eta}{\partial t} + \nabla \cdot (\mathbf{v}\eta) + \frac{\partial}{\partial \sigma} (S_\sigma \eta) = 0 \tag{3}$$

9

where η is the mass density in $x - y - \sigma$ space, $\mathbf{v}$ is the horizontal wind in this space, and $S_\sigma = d\sigma/dt$ is the vertical velocity in σ coordinates.

Momentum:

$$\frac{\partial \mathbf{u}}{\partial t} + \nabla \cdot (\mathbf{v}\mathbf{u} - K_h \nabla \mathbf{v}) + \frac{\partial}{\partial \sigma}\left(S_\sigma \mathbf{u} - K_\sigma \frac{\partial \mathbf{v}}{\partial \sigma}\right) + \eta \nabla M - \eta \Pi \nabla \theta + f \mathbf{k} \times \mathbf{u} = \eta \mathbf{S}_v \quad (4)$$

where $\mathbf{u} = \eta \mathbf{v}$, M is the Montgomery potential, Π is the Exner function, $f = \beta y$ is the Coriolis parameter, and K_h and K_σ are the horizontal and vertical eddy mixing coefficients.

Water substance:

$$\frac{\partial \eta_t}{\partial t} + \nabla \cdot (\mathbf{v}\eta_t - K_h \nabla r_t) + \frac{\partial}{\partial \sigma}\left(S_\sigma \eta_t - K_\sigma \frac{\partial r_t}{\partial \sigma}\right) = \eta S_r \quad (5)$$

where r_t is the total cloud water (vapor plus advected condensate) mixing ratio and $\eta_t = \eta r_t$.

The σ coordinate vertical velocity is

$$S_\sigma = \frac{d\sigma}{dt} = \frac{S_\theta - (1 - \sigma)(S_B + \Delta \mathbf{v}_B \cdot \nabla \theta_B)}{\theta_T - \theta_B}, \quad (6)$$

where $S_\theta = d\theta/dt$, S_B is S_θ at the surface, and $\Delta \mathbf{v}_B = \mathbf{v} - \mathbf{v}_B$, with $\mathbf{v}_B$ being $\mathbf{v}$ at the surface.

The horizontal and vertical eddy mixing coefficients are given by

$$K_h = \eta C_K \left[\left(\frac{\partial v_x}{\partial x}\right)^2 + \left(\frac{\partial v_y}{\partial y}\right)^2 + \frac{1}{2}\left(\frac{\partial v_x}{\partial y} + \frac{\partial v_y}{\partial x}\right)^2\right] \Delta x \Delta y \quad (7)$$

and

$$K_\sigma = \eta C_K \left|\frac{\partial S_\sigma}{\partial \sigma}\right| (\Delta \sigma)^2 \quad (8)$$

where Δx, Δy, and $\Delta \sigma$ are the x, y, and σ cell sizes and where $C_K = 1$.

The Montgomery potential is defined

$$M = \theta\Pi + \Phi, \tag{9}$$

where Φ is the geopotential.

The pressure p can be obtained from the hydrostatic equation in σ coordinates

$$\frac{\partial p}{\partial \sigma} = -g\eta \tag{10}$$

subject to the upper boundary condition of fixed pressure at the top of the domain. The Exner function is related to the pressure by

$$\Pi = C_p(p/p_R)^\kappa \tag{11}$$

where p_R is a constant reference pressure and $\kappa = (C_p - C_v)/C_p$ with C_p and C_v being the specific heats at constant pressure and volume. Finally, the Montgomery potential is obtained from the identity $dM = d(\theta\Pi) + d\Phi = \Pi d\theta + \theta d\Pi + d\Phi$ and the hydrostatic equation written in the form $\theta d\Pi = -d\Phi$,

$$\frac{\partial M}{\partial \sigma} = (\theta_T - \theta_B)\Pi \tag{12}$$

subject to the condition at the surface

$$M_B = \theta_B\Pi_B + gh, \tag{13}$$

where g is the acceleration of gravity and $h(x,y)$ is the height of the terrain, taken here to be zero. The geopotential is obtained by solving equation (9),

$$\Phi \equiv gz = M - \theta\Pi \tag{14}$$

where z is the height above the zero level.

The surface potential temperature is governed by

$$\frac{\partial \theta_B}{\partial t} + \mathbf{v}_B \cdot \nabla \theta_B = S_B. \tag{15}$$

3.2 Diabatic and frictional parameterizations

The toy convective and surface flux parameterizations of Raymond (2007) are used with modifications discussed below, as is the toy radiation scheme of Raymond and Torres (1998) and Raymond (2000), to determine the source terms for momentum and moisture $\mathbf{S}_v$, S_θ, and S_r. The convective scheme is a kind of convective adjustment in which the adjustment is done as a relaxation over the full vertical depth of the convective layer, as defined by the height of undilute neutral buoyancy from the planetary boundary layer. Surface fluxes are obtained using simple bulk flux formulas. For convenience, the convective and surface flux parameterizations are presented in appendix A.

The radiation scheme is quite crude, but is tuned roughly to the scheme used in the National Center for Atmospheric Research's Community Climate Model version 2 (Kiehl et al. 1994).

Two small but significant changes are made in the cumulus parameterization relative to the version presented by Raymond (2007). In that version the deep convective adjustment rate a is assumed to be constant. (Note that a is called η in Raymond (2007), but this clashes with the definition of σ coordinate air density in the present paper.) However, one would expect adjustment to take place more rapidly in intensely convective regimes than in regimes with weaker convection. We find that precipitation is a strong function of tropospheric humidity, and therefore take the saturation fraction H (33) to be a proxy for strong convective mixing. The deep convective adjustment rate a (32) is thus made proportional to H^s where s is a constant. The form (humidity)^s also appears in the source term for convective precipitation, and comparison of the current version of the cumulus

12

parameterization with the CRM of Raymond (2007) suggests a value $s = 6$, which makes both convective precipitation and mixing strongly increasing functions of tropospheric humidity.

The other change is to the vertical dependence of the source term for convective precipitation $\mu(z)$. This is made small at low levels in order to avoid the production of strong precipitation from shallow clouds. A somewhat smoother form than previously used is defined in the current version of the parameterization by (35).

Raymond (2007) showed that comparison of a parameterization with a CRM in the context of the weak temperature gradient approximation provides a rational means for tuning a parameterization – constants are adjusted until a reasonable fit between the CRM and the parameterization is obtained. As shown in figure 3 the predicted saturation fraction as a function of wind speed for the current parameterization is much less at low wind speeds than that of Raymond (2007), due primarily to the addition of a mixing coefficient which depends on saturation fraction.

3.3   Numerical considerations

As in Raymond (2001, 2007), (3)-(5) are integrated using Lax-Wendroff differencing, while the surface potential temperature equation employs simple upstream differencing. The simplicity of the latter is justified because the surface potential temperature is governed primarily by local effects in the tropics, with only secondary tendencies due to advection. The eddy mixing coefficients K_h and K_σ are augmented above $\sigma = 0.8$ to produce a sponge layer at the top of the domain to absorb upward-propagating waves. Also as in Raymond (2007), cloud-radiation interactions are turned off in order to eliminate this source of variability. A small amount of initial variance is introduced into simulations by making random perturbations to the initial humidity field at low levels.

In addition to smoothing from eddy mixing, weak fourth-order vertical smoothing is done on η, $\mathbf{u}$, and η_t in order to suppress the short vertical wavelength computational mode to

which cell-centered calculations are subject. This takes the form

$$\tilde{\chi}_i = (1 - \lambda_V)\chi_i + \lambda_V \left[\frac{2}{3}(\chi_{i+1} + \chi_{i-1}) - \frac{1}{6}(\chi_{i+2} + \chi_{i-2})\right] \tag{16}$$

for each variable χ where the tilde indicates the smoothed variable, the subscript indicates the vertical level, and $\lambda_V = 0.01$. Symmetric mirror conditions are used at the surface and top to insure conservation. The horizontal fourth-order smoothing used by Raymond (2007) was also eliminated here as it was found to be unnecessary with the changes in the cumulus parameterization mentioned above. Version sigma-066 of the model is used for the computations in this paper.

3.4   Definition of NGMS

We define the normalized gross moist stability (NGMS) for the output of this model following Raymond and Sessions (2007):

$$\Gamma_R = -\frac{T_R[\nabla \cdot (\eta s \mathbf{v})]}{L[\nabla \cdot (\eta r_t \mathbf{v})]} \tag{17}$$

where $T_R = 300$ K is a constant reference temperature, L is the latent heat of condensation plus freezing, and the square brackets indicate an integral in σ from 0 to 1. The variable s is the moist entropy and r_t is the total cloud water mixing ratio. We further subdivide this into two pieces, a part having to do with horizontal entropy advection,

$$\Gamma_{R1} = -\frac{T_R[\eta \mathbf{v} \cdot \nabla s]}{L[\nabla \cdot (\eta r_t \mathbf{v})]}, \tag{18}$$

and a part associated with vertical advection, which is more closely related to the Neelin-Held (1987) definition of gross moist stability:

$$\Gamma_{R2} = -\frac{T_R[s\nabla \cdot (\eta \mathbf{v})]}{L[\nabla \cdot (\eta r_t \mathbf{v})]} \approx -\frac{T_R[\eta S_\sigma(\partial s/\partial \sigma)]}{L[\nabla \cdot (\eta r_t \mathbf{v})]}. \tag{19}$$

14

The approximation in this equation comes from neglecting the time derivative in the mass continuity equation (3) and then integrating by parts in σ. The denominator in (17) is equal to the latent heating associated with moisture convergence. Following Back and Bretherton (2006), we denote $T_R[\eta \mathbf{v} \cdot \nabla s]$ the "horizontal advection" part of the entropy divergence and $T_R[\eta S_\sigma(\partial s/\partial \sigma)]$ the "vertical advection" part.

It is a bit awkward to have two possibly conflicting definitions of NGMS in (1) and (17). However, the differences in these definitions are less than they appear to be at first sight. First, the linearized model of section 2 does not admit horizontal advection in the moving reference frame of the mean flow. It is thus omitted from the definition of NGMS in (1). Second, the difference between normalization in terms of mixing ratio rather than dry entropy is small. This is because L times the moisture removed from a parcel passing through a convective system approximately equals T_R times the specific dry entropy added to the parcel, assuming that the parcel conserves moist entropy. Thus, $\Gamma_{R2} \approx \Gamma_M$.

4   Toy model results

4.1   Moisture modes over uniform SST

We first examine the development of moisture modes in the toy model under conditions of uniform SST, zero ambient wind, no rotation, and varying spatial resolution of 250 km, 125 km, 62.5 km, and 31.25 km. In all cases a domain of 5000 km $\times$ 5000 km is used in the horizontal with doubly periodic boundary conditions. In the vertical, 20 levels are used, equally spaced in σ. The simulation is initiated with a single column radiative-convective equilibrium profile with random humidity perturbations at low levels. All simulations were run for a minimum of 5000 ks or about 58 d. Figure 4 shows rainfall rate, saturation fraction, and surface winds for these simulations at 2500 ks into the simulation.

The simulations show that a cellular convective structure develops for each of the model resolutions. As model grid size increases, the representation of fine-scale detail decreases

as expected. Due to the different random initializations the resulting convective patterns differ for the different resolutions. However, the size of convectively active patches ($\approx$ $500 - 1000$ km) and the spacing of convective cells (≈ 2000 km) remain the same for grid resolutions as coarse as 125 km; only for the 250 km case do these dimensions increase. This suggests that a grid size of 125 km is sufficient to capture the basic cellular structure of convection in this model, though of course finer scale detail is unresolved.

This is to be compared with the CRM results of Bretherton et al. (2005) on a 576×576 km domain. Self-aggregation occurred in this case, producing convectively active patches of order 100 km in diameter, with typically only one patch existing in the model domain. This contrasts with patches $5 - 10$ times bigger in our case. However it is unclear whether the convectively active regions would have grown to larger sizes in Bretherton et al.'s CRM if it had been possible to use a larger model domain. Thus, at this point we cannot say what the scales of convective patches and their surrounding subsidence regions are in nature.

4.2   Reynolds SST aquaplanet simulations

In this section idealized aquaplanet simulations with 125 km grid resolution are made in which the sea surface temperature distribution is taken from the global synthesis of SST by Reynolds and Marsico (1993). In this synthesis the SST is interpolated across continents. We are thus ignoring the vast difference between land-air and sea-air interactions, which is why we characterize our results as "idealized". However, the MJO manifests itself largely in the oceanic domain, so it should be possible to learn something about the MJO in this semi-realistic context without having to delve into the complex processes which occur in the atmosphere over land. Clearly, interactions of the MJO with the Asian monsoon will not be represented correctly in these simulations.

Another idealized aspect of the simulations is the use of an equatorial beta plane to represent the tropical and near-tropical regions of the earth. The model domain is taken to be 40000 km in the zonal direction by 12000 km in the meridional direction with periodic

east-west boundary conditions and free slip walls bounding the simulations to the north and south. Twenty vertical levels are used as in the last section.

Simulations are run for 50000 ks or about 579 d. The Reynolds SSTs are scaled to an earth with a circumference of 40000 km. In order to minimize spurious baroclinic wall disturbances at high latitudes, the SST is bounded below by 15° C.

Two simulations are reported, with perpetual February and August SSTs respectively. Figure 5 shows the SST distributions used in the model in both cases as well as the intraseasonal rainfall variance in each case. The latter is defined as the variance of the rainfall rate field over the time interval $20000 - 45000$ ks after application of a temporal band pass filter of $7 - 90$ d and a longitudinal low pass filter with smoothing length of 3000 km. There is fair agreement with the analysis of observations by Zhang (2005), though the northern summer shows stronger rainfall variance than the southern summer and the northern summer variance in the eastern Pacific and western Atlantic is too strong in the simulations. Perhaps these differences can be explained at least in part by the lack of land in the simulations.

Figures 6 and 7 show Hovmöller diagrams for surface zonal wind and precipitation in equatorial regions south and north of the equator for perpetual February and August simulations respectively. Low pass filtering on longitude (3000 km smoothing length) and time (7 d smoothing time) has been performed to isolate intraseasonal disturbances. Eastward propagation of westerly wind and precipitation anomalies is clearly seen in both cases over the Indo-Pacific warm pool with broadly distributed propagation speeds ranging from about 1 m s^{-1} to 8 m s^{-1}. Higher speeds are typically seen in the February case. The February disturbances show more power at higher frequencies than do the August disturbances. In August the disturbances disappear near the dateline (20000 km) and reappear in the east Pacific as is observed, whereas in February disturbances continue somewhat further east into the southeast Pacific convergence zone, but with no separate east Pacific signal.

Figure 8 shows two snapshots of the rainfall rate, the surface wind, and the saturation fraction over the northern part of the Indo-Pacific warm pool. The first snapshot is taken

during a convectively quiescent period in this region, while the second shows a convectively active period. The strongest convection in the latter case takes the form of a continuous intertropical convergence zone (ITCZ) distorted by breaking wave disturbances. The surface winds in equatorial regions are much stronger in the active case, with strong westerlies coincident with the heavy precipitation. The disturbances have the apparent character of westerly wind bursts (Lau et al. 1989; Fasullo and Webster 2000). These disturbances generally move to the east, as does the entire pattern of strong convection. It is this latter pattern, consisting in general of one or more westerly wind bursts and the associated active ITCZ that constitutes the MJO-like disturbance.

The simulated disturbance in our model satisfies most of the criteria for the MJO listed in the introduction. In particular:

1. The disturbance is global in scale, convectively coupled, and moves to the east at about the right speed. The associated convection is strongest over the Indo-Pacific warm pool.

2. The disturbance has a first baroclinic mode structure in the vertical and Gill model structure in the horizontal, with low-level westerlies in the equatorial region.

3. The overall MJO-like disturbance consists of multiple disturbances of smaller scale.

4. The convection follows the latitudinal excursions of the SST.

However, the convective heating does not tilt consistently to the west with height and the surface westerlies coincide with precipitation in the Indian Ocean region as well as the west Pacific rather than being displaced to the west.

4.3   NGMS in the toy model

We now turn to a diagnosis of the NGMS exhibited by the convection in the simulated MJO, focusing on the convection in the Indo-Pacific warm pool in the perpetual August simulation.

We average the numerators and denominators of (18) and (19) over the region $12000 < x <$ 18000 km, $0 < y < 1500$ km, which covers the heart of the region of intraseasonal variability shown in the lower panel of figure 5.

Figure 9 shows scatter plots of the horizontal ($T_R[\eta \mathbf{v} \cdot \nabla s]$) and vertical ($T_R[\eta S_\sigma (\partial s / \partial \sigma)]$) advective parts of the entropy divergence vs. the moisture convergence ($-L[\nabla \cdot (\eta r_t \mathbf{v})]$), with each point representing a snapshot of these quantities averaged over the Indo-Pacific warm pool as indicated above. For positive moisture convergence figure 9 shows that horizontal advection generally results in entropy divergence, tending to decrease the average entropy. On the other hand, vertical advection in the model tends to increase the entropy in the column. The former effect is stronger, so overall entropy divergence and the NGMS are positive. Quantitatively, we find that time-averaging the moisture convergence and the pieces of the entropy divergence results in $\Gamma_{R1} = 0.90$, $\Gamma_{R2} = -0.20$, and $\Gamma_R = 0.70$ for this region.

The positive value of Γ_R means that on the average entropy is laterally exported from the Indo-Pacific warm pool in our model. However, the horizontal advection part of the entropy divergence is not Galilean-invariant; viewing this quantity in a reference frame moving with a convective disturbance could potentially yield a much smaller value for the contribution of horizontal advection to the entropy divergence, especially if the disturbance drifts with the wind in a region of low vertical shear. This is likely to happen with moisture modes, which tend to move at a speed close to that of the wind. On the other hand, the vertical advection term is Galilean-invariant, so its value would not change in a moving reference frame. It is thus an intrinsic property of the convection.

We hypothesize that the MJO-like disturbances appearing over the warm pool in our model are moisture modes, and are therefore dependent on the existence of negative values of Γ_{R2}.

5 NGMS in the FNL

The analysis system used to initialize the Global Forecast System (GFS) model of the National Centers for Environmental Prediction (NCEP) is called the Final Analysis (FNL). Though the FNL and GFS are spectral models with a sigma vertical coordinate, the FNL data are made available in 1° grid form on pressure levels. The FNL is a variational analysis system in which the previous GFS model output is used in conjunction with observations to derive an initialization for the next GFS run (Parrish and Derber 1992). Over tropical oceans where conventional observations are sparse, vertical velocity profiles and other aspects of analysis data should be determined largely by GFS physical parameterizations. However, the location, structure, and intensity of large-scale convectively coupled systems such as the MJO should appear in the analysis whether or not the GFS supports such systems in free running mode. Jia-Lin Lin (personal communication 2008) concludes that in common with many other global atmospheric models (Lin et al. 2006), the GFS does not satisfactorily simulate the MJO.

Figure 10 shows the moisture convergence in the FNL averaged over $0° - 15°$ N for June through September 2005. Two MJO events are evident in the western Pacific during this period, one near day 210, the other near day 250. Eastward propagation is evident in both of these events from the Indian Ocean to the eastern Pacific.

Figure 11 shows the outgoing longwave radiation (OLR) for the same period and latitudinal average. Comparison with figure 10 shows that low OLR values roughly correspond with regions of strong moisture convergence in the FNL, indicating that the FNL is indeed seeing major convectively coupled disturbances in the tropical regions.

Since FNL data are presented on pressure levels, the definition of the NGMS Γ_R must be modified accordingly. In analogy with (18) and (19), we define the horizontal advection part of Γ_R as

$$\Gamma_{R1} = -\frac{T_R[\mathbf{v} \cdot \nabla s]}{L[\nabla \cdot (r_t \mathbf{v})]} \tag{20}$$

and the vertical advection part as

$$\Gamma_{R2} = -\frac{T_R[\omega(\partial s/\partial p)]}{L[\nabla \cdot (r_t \mathbf{v})]} \tag{21}$$

in pressure coordinates, where the square brackets now indicate an integral over the range $100 - 1000$ hPa.

Figure 12 shows daily average FNL values over June-September 2005 of the horizontal and vertical advection parts of the entropy divergence vs. the moisture divergence over the Indo-Pacific warm pool. In agreement with figure 9, the averaging domain is $108° - 162°$ in longitude and $0° - 14°$ in latitude.

Unlike our toy model results, both the horizontal and vertical advective parts of the moist entropy divergence are positive, with $\Gamma_{R1} = 0.25$, $\Gamma_{R2} = 0.21$, and $\Gamma_R = 0.47$, implying positive NGMS. These results, which differ fundamentally from those of our toy model, are almost certainly a function of GFS/CFS/FNL model physics and not a result of observations, which are sparse over tropical oceans. We conclude that the GFS/CFS model is unable to support moisture modes over the Indo-Pacific warm pool, at least without strong surface flux and cloud-radiative forcing, and hypothesize that the inability of the GFS/CFS to simulate the MJO is related to this fact.

6   Discussion and conclusions

In this paper we explore the hypothesis that the Madden-Julian oscillation is driven by moisture mode instability. For this mode to function, the precipitation rate must be a strong positive function of the saturation fraction. In addition, the deep convection which produces the precipitation must act to further moisten the atmosphere. Generally, a negative value of the normalized gross moist stability (NGMS) is needed for such moistening to occur. However, regions of enhanced precipitation often exhibit enhanced surface entropy fluxes due to enhanced winds and gustiness and suppressed tropopause fluxes associated with

21

the reduction in outgoing longwave radiation by high stratiform cloudiness. In these cases moistening of the column can occur with weakly positive values of the NGMS. Note that in contrast to (Raymond 2001), cloud-radiation interactions are not considered in this paper.

The moisture mode is illustrated in its simplest form by the linearized model of Raymond and Fuchs (2007). In the simplest manifestation of this model surface and tropopause entropy flux anomalies are ignored and moisture modes amplify only if the NGMS is negative. In the linear case these modes are stationary (or move with the ambient wind) unless some other factor such as wind-induced surface heat exchange in the presence of an ambient surface flow exists. The growth rate of these modes tends to be relatively independent of scale except that some decrease in growth rate occurs for very long wavelengths. The results of Bretherton et al. (2005) show that the growth of moisture modes, represented in that paper by the self-aggregation of convection, is possible in cloud-resolving numerical models, even though the profile of lateral inflow and outflow of entropy in this model differs from the simple linearized case.

We show that the toy large-scale model of Raymond (2007) also exhibits self-aggregation of convection in the simplified context of a three-dimensional doubly periodic domain with uniform SST and no rotation. In this model the NGMS consists of two parts, one associated with the tropospheric-average horizontal advection of moist entropy, the other with its average vertical advection. The former can be thought of as a ventilation term in which the moist entropy in the core of a convective region is reduced by dry advection, whereas the latter is closely related to the Neelin-Held (1987) form of the gross moist stability.

It is noteworthy that self-aggregation occurs in the present model even in the absence of cloud-radiation interactions, a process that was central to the results of Raymond (2001). The stronger response of precipitation to saturation fraction in the current version of the cumulus parameterization is responsible for this change.

The toy model produces robust MJO-like disturbances on an aquaplanet with Reynolds SST distributions for February and August. These disturbances exhibit many of the charac-

teristics of the MJO as outlined by Zhang (2005). In these simulations the vertical advection part of the NGMS over the Indo-Pacific warm pool is on the average negative, whereas the horizontal advection part is positive, at least when evaluated in the earth's reference frame. Since the horizontal advection is highly variable and can be reduced greatly in the moving reference frame of the disturbance where the relative wind is small, moisture mode instabilities can develop. We hypothesize that the MJO produced in the model and in the real world are both fundamentally driven by this moisture mode instability.

Further evidence for this view is provided by the final analysis (FNL) of NCEP's Global Forecast System (GFS) and the associated Climate Forecast System (CFS). The GFS/CFS produces only a weak MJO. Diagnosis of the FNL shows positive values for both parts of the NGMS over the Indo-Pacific warm pool. Since observational data are likely to be insufficient to constrain mass flux profiles in the FNL over tropical oceans, these profiles and the associated vertical entropy advection are likely to be governed by model physics. We hypothesize that the absence of an MJO in the CFS is due to the fact that the vertically averaged vertical moist entropy advection is positive in the model, thus leading to the suppression of moisture modes in the absence of strong surface and tropopause entropy flux anomalies coupled to precipitation.

It would be desirable to diagnose other global models in the above manner in order to determine whether the relationship between negative gross moist stability and MJO formation exists in them as well.

In summary, the theoretical and modeling work in this paper suggests that the Madden-Julian oscillation is driven by moisture mode instability. However, much remains to be revealed about the detailed workings of moisture mode dynamics in this prominent but elusive phenomenon.

Appendix A – Cumulus parameterization

The cumulus parameterization is an adjustment scheme, with separate calculations made for shallow and deep convection. The forms of the convective source terms for each type of convection are the same; for equivalent potential temperature θ_e, total cloud water mixing ratio r_t, and the horizontal velocity $\mathbf{v}$, they are

$$S_{eci} = \left(\bar{\theta}_e - \theta_e(z) + \frac{F_e}{M} \right) a(z) \tag{22}$$

$$S_{ri} = \left(\bar{r}_t - r_t(z) + \frac{F_r}{M} \right) a(z) - C_R(z) \tag{23}$$

$$\mathbf{S}_{vi} = \left(\bar{\mathbf{v}} - \mathbf{v}(z) + \frac{\mathbf{F}_v}{M} \right) a(z) \tag{24}$$

where F_e, F_r, and $\mathbf{F}_v$ are the surface fluxes of the corresponding variables.

The overbar applied to any variable $\chi(z)$ is

$$\bar{\chi} = \frac{1}{M} \int_0^D \rho(z) a(z) \chi(z) dz \tag{25}$$

where $\rho(z)$ is the atmospheric density profile, D is the depth of the convective layer, and where

$$M = \int_0^D \rho(z) a(z) dz. \tag{26}$$

Equations (22)-(24) are designed so that, for instance,

$$\int_0^D \rho(z)(\bar{\theta}_e - \theta_e) a(z) dz = 0, \tag{27}$$

so that the first two terms represent a conservative redistribution or adjustment which attempts to homogenize vertically the variable in question. The third term on the right of these equations represents the vertical distribution of surface fluxes. This distribution is weighted by the rate function $a(z)$, the form of which is discussed below.

The subscripted i on the left sides of the above equations equals either d for deep convection or s for shallow convection. The two convective regimes are assumed to exist simultaneously in varying proportions. Actual profiles of convective source terms are computed as weighted averages of the shallow and deep convective profiles, indicated respectively by subscripted s and d:

$$S_{ec} = \epsilon S_{ecd} + (1 - \epsilon) S_{ecs} \qquad (28)$$

etc.

Observations over warm tropical oceans generally show positive buoyancy for planetary boundary layer (PBL) parcels everywhere in the troposphere except for a stable layer just above the PBL. The partitioning between shallow and deep convection in each grid box is decided on the basis of the convective inhibition in this layer. The parameter ϵ is a measure of this inhibition:

$$\epsilon = \mathcal{T}(\theta_{eb} - \theta_{et}, \Delta \theta_e), \qquad (29)$$

where $\Delta \theta_e$ is a constant, θ_{eb} is the mean equivalent potential temperature in the height range $0 < z < b$ where b is the fixed PBL depth and θ_{et} is the mean saturated equivalent potential temperature in the range $b < z < 2b$. The function $\mathcal{T}(x, y)$ is a throttle function, i. e.,

$$\mathcal{T}(x, y) = \begin{cases} 0, & x < -y/2 \\ x/y + 1/2, & -y/2 < x < y/2 \\ 1, & x > y/2 \end{cases} \qquad (30)$$

For shallow PBL convection we define the rate function as

$$a(z) = \lambda_c (1 - z/b) \Lambda(b - z) \qquad \text{(shallow)} \qquad (31)$$

where λ_c represents the maximum mixing rate and the function $\Lambda(x) = \lim_{y \to 0} \mathcal{T}(x, y)$. Precipitation production and evaporation in shallow convection is assumed to take the same

form as in deep convection (see below), though the precipitation rate in the shallow case tends to be very small or zero.

For the deep convective regime the rate function $a(z)$ equals

$$a(z) = \lambda_c H^s \Lambda(D - z) \qquad \text{(deep)} \tag{32}$$

where s is a constant called the stiffness parameter. The stiffness parameter determines the "stiffness" of the relationship between humidity on one hand and convective mixing and precipitation rate on the other. The convective layer depth D is assumed to be the height of the level of neutral buoyancy for parcels with average characteristics of the PBL. In calculating D, the highest level of neutral buoyancy is taken for these parcels, thus ignoring possible inversions and stable layers at intermediate altitudes. The saturation fraction H is defined

$$H = \int_0^\infty \rho r_t dz \Big/ \int_0^\infty \rho r_s dz \ . \tag{33}$$

The vertical profile $C_R(z)$ represents the conversion of total cloud water (vapor plus cloud droplets) to precipitation, and it takes a rather complex form

$$C_R = \lambda_p (r_v/r_s)^s \mu(z) + \lambda_s (r_t - r_s) \Lambda(r_t - r_s) \mathcal{T}(\Gamma - \Gamma_t, \Gamma_s) - \lambda_e (r_s - r_t) \Lambda(r_s - r_t) r_p \tag{34}$$

involving three terms. The third term represents the evaporation of precipitation. The quantities r_s and r_p are the saturation and precipitation mixing ratios and λ_e is a constant controlling the evaporation rate.

The second term represents the formation of precipitation in regions that are saturated on the large scale, and λ_s is the rate constant controlling this process. The quantity $\Gamma = d\theta_e/dz$ and Γ_t is a constant threshold value of Γ, while Γ_s defines the range over which the throttle function turns on. The purpose of the throttle function in the second term of (34) is to suppress the conversion of cloud water to precipitation in saturated regions where $\Gamma < 0$.

Since grid-scale saturation with negative Γ is unstable, it cannot exist for long. Such regions are interpreted as being mainly unsaturated, but pierced by saturated columns of convection of sufficient density to render the average cloud water content saturated. The instability in this case resides solely in the convective columns, and it is inappropriate to turn on "stratiform" processes in this case.

The first term represents the conversion of cloud water to precipitation by convective columns in regions which may or may not be saturated on the grid scale. This process is governed by the rate constant λ_p. The process is assumed to be proportional to the relative humidity r_v/r_s to the power s (the stiffness parameter used in (32)), where r_v is the water vapor mixing ratio. It is rate-limited to a value such that $C_{Rp}\Delta t < 0.3 r_t/s$ in order to avoid relaxation oscillations. The quantity C_{Rp} is that part of C_R associated with convective precipitation production and Δt is the time step.

The function $\mu(z)$ takes the assumed form

$$\mu(z) = \{1 - \exp[-(z/z_p)^2]\}\Lambda(D - z). \tag{35}$$

It thus causes convective precipitation formation to turn on gradually with height, with the scaling being governed by z_p. In any case, convective precipitation is not allowed above the convective top $z = D$. In addition, if the convective precipitation term as calculated above removes more than 30% of r_t in a single time step, it is limited to this 30% magnitude, thus suppressing unphysical oscillations in the simulation.

The vertical profile of precipitation rate $P = \rho w_t r_p$ is assumed to adjust instantly to conditions in the grid box, and thus obeys the time-independent vertical advection equation

$$\frac{1}{\rho}\frac{\partial P}{\partial z} = -C_R, \tag{36}$$

subject to $P = 0$ at the top of the domain. Thus, integrating (36) down from the top yields the precipitation rate at the surface.

A simplified definition of equivalent potential temperature is used in this parameterization:

$$\theta_e = \theta \exp(\gamma r_t), \tag{37}$$

where $\gamma = L/(C_p T_R)$, $L = L_c + L_f$ being the sum of the latent heats of condensation and freezing, C_p the specific heat of air at constant temperature, and $T_R = 300$ K a constant reference temperature. The total cloud water mixing ratio r_t is used instead of the vapor mixing ratio, because the difference between the two is likely to be small when averaged over grid boxes typical of large-scale models.

The potential temperature source term is computed from the equivalent potential temperature and total water source terms using

$$S_\theta = \theta[(S_{ec} + S_{er})/\theta_e - \gamma S_r] \tag{38}$$

where S_{ec} and S_{er} are the convective and radiative contributions to the equivalent potential temperature source, S_r is the convective source of total water mixing ratio, and γ is defined above. The total precipitation rate is the weighted average of the deep and shallow rates:

$$P = \epsilon P_d + (1 - \epsilon) P_s. \tag{39}$$

Surface fluxes for each variable χ are calculated using a simple bulk formula:

$$F_\chi = \mathcal{T}(T_{ss} - T_b, \Delta T)\rho_b C_D(|\mathbf{v}_b|^2 + W^2)^{1/2}(\chi_{ss} - \chi_b) \tag{40}$$

where T_{ss} is the temperature of the sea surface, T_b is the temperature of the air in the boundary layer adjacent to the surface, ΔT and W are a constants, C_D is the (constant) drag coefficient, a subscripted b indicates a boundary layer value, and a subscripted ss indicates a sea surface value. The throttle function turns the fluxes off when $T_b > T_{ss} + \Delta T/2$.

Table 1 lists values of parameters used in the cumulus parameterization.

28

References

Back, L, E., and C. S. Bretherton, 2006: Geographic variability in the export of moist static energy and vertical motion profiles in the tropical Pacific. *Geophys. Res. Letters*, **33**, L17810, doi:10.1029/2006GL026672.

Bretherton, C. S., M. E. Peters, and L. E. Back, 2004: Relationships between water vapor path and precipitation over the tropical oceans. *J. Climate,* **17,** 1517-1528.

Bretherton, C. S., P. N. Blossey, and M. Khairoutdinov, 2005: An energy-balance analysis of deep convective self-aggregation above uniform SST. *J. Atmos. Sci.,* **62,** 4273-4292.

Derbyshire, S. H., I. Beau, P. Bechtold, J.-Y. Grandpeix, J.-M. Piriou, J.-L. Redelsperger, and P. M. M. Soares, 2004: Sensitivity of moist convection to environmental humidity. *Quart. J. Roy. Meteor. Soc.,* **130,** 3055-3079.

Emanuel, K. A., 1986: An air-sea interaction theory for tropical cyclones: Part I: Steady state maintenance. *J. Atmos. Sci.,* **43,** 585-604.

Emanuel, K. A., 1987: An air-sea interaction model of intraseasonal oscillations in the tropics. *J. Atmos. Sci.,* **44,** 2324-2340.

Fasullo, J., and P. J. Webster, 2000: Atmospheric and surface variations during westerly wind bursts in the tropical western Pacific. *Quart. J. Roy. Meteor. Soc.,* **126**, 899-924.

Fuchs, Z., and D. J. Raymond, 2002: Large-scale modes of a nonrotating atmosphere with water vapor and cloud-radiation feedbacks. *J. Atmos. Sci.,* **59,** 1669-1679.

Fuchs, Z., and D. J. Raymond, 2005: Large-scale modes in a rotating atmosphere with radiative-convective instability and WISHE. *J. Atmos. Sci.,* **62,** 4084-4094.

Fuchs, Z. and D. J. Raymond, 2007: A simple, vertically resolved model of tropical disturbances with a humidity closure. *Tellus*, **59A**, 344-354.

Gill, A. E., 1980: Some simple solutions for heat-induced tropical circulation. *Quart. J. Roy. Meteor. Soc.,* **106,** 447-462.

Grabowski, W. W., 2001: Coupling cloud processes with the large-scale dynamics using the cloud-resolving convection parameterization (CRCP). *J. Atmos. Sci.,* **58,** 978-997.

Grabowski, W. W., 2003: MJO-Like coherent structures: Sensitivity simulations using the cloud-resolving convection parameterization (CRCP). *J. Atmos. Sci.,* **60,** 847-864.

Khairoutdinov, M., D. Randall, and C. DeMott, 2005: Simulations of the atmospheric general circulation using a cloud-resolving model as a superparameterization of physical processes. *J. Atmos. Sci.,* **62,** 2136-2154.

Kiehl, J. T., J. J. Hack, B. P. Briegleb, 1994: The simulated Earth radiation budget of the National Center for Atmospheric Research community climate model CCM2 and comparisons with the Earth Radiation Budget Experiment (ERBE). *J. Geophys. Res.,* **99,** 20815-20827.

Lau, K. M., L. Peng, C. H. Sui, and T. Nakazawa, 1989: Dynamics of super cloud clusters, westerly wind bursts, 30-60 day oscillations and ENSO: A unified view. *J. Meteor. Soc. Japan,* **67**, 205-219.

Lin, J.-L., G. N. Kiladis, B. E. Mapes, K. M. Weickmann, K. R. Sperber, W. Lin, M. C. Wheeler, S. D. Schubert, A. Del Genio, L. J. Donner, S. Emori, J.-F. Gueremy, F. Hourdin, P. J. Rasch, E. Roeckner, and J. F. Scinocca, 2006: Tropical intraseasonal variability in 14 IPCC AR4 climate models. Part I: Convective signals. *J. Climate,* **19,** 2665-2690.

López Carrillo, C., and D. J. Raymond, 2005: Moisture tendency equations in a tropical atmosphere. *J. Atmos. Sci.,* **62,** 1601-1613.

Lucas, C., E. J. Zipser, and B. S. Ferrier, 2000: Sensitivity of tropical west Pacific oceanic squall lines to tropospheric wind and moisture profiles. *J. Atmos. Sci.,* **57,** 2351-2373.

Mapes, B. E., 2004: Sensitivities of cumulus-ensemble rainfall in a cloud-resolving model with parameterized large-scale dynamics. *J. Atmos. Sci.,* **61,** 2308-2317.

Neelin, J. D., and I. M. Held, 1987: Modeling tropical convergence based on the moist static energy budget. *Mon. Wea. Rev.,* **115,** 3-12.

Parrish, D. F., and J. C. Derber, 1992: The National Meteorological Center's spectral statistical-interpolation analysis system. *Mon. Wea. Rev.,* **120,** 1747-1763.

Raymond, D. J., 2000: The Hadley circulation as a radiative-convective instability. *J. Atmos. Sci.,* **57,** 1286-1297.

Raymond, D. J., 2001: A new model of the Madden-Julian oscillation. *J. Atmos. Sci.,* **58,** 2807-2819.

Raymond, D. J., 2007: Testing a cumulus parametrization with a cumulus ensemble model in weak-temperature-gradient mode. *Quart. J. Roy. Meteor. Soc.,* **133,** 1073-1085.

Raymond, D. J., and A. M. Blyth, 1986: A stochastic mixing model for nonprecipitating cumulus clouds. *J. Atmos. Sci.,* **43,** 2708-2718.

Raymond, D. J., and Z. Fuchs, 2007: Convectively coupled gravity and moisture modes in a simple atmospheric model. *Tellus,* **59A**, 627-640.

Raymond, D. J. and S. L. Sessions, 2007: Evolution of convection during tropical cycloge-nesis. *Geophys. Res. Letters*, **34**, L06811, doi:10.1029/2006GL028607.

Raymond, D. J., S. L. Sessions, and Z. Fuchs, 2007: A theory for the spinup of tropical depressions. *Quart. J. Roy. Meteor. Soc.,* **133,** 1743-1754.

Raymond, D. J., and D. J. Torres, 1998: Fundamental moist modes of the equatorial troposphere. *J. Atmos. Sci.,* **55,** 1771-1790.

Raymond, D. J., and X. Zeng, 2005: Modelling tropical atmospheric convection in the context of the weak temperature gradient approximation. *Quart. J. Roy. Meteor. Soc.,* **131,** 1301-1320.

Reynolds, R. W., and D. C. Marsico, 1993: An improved real-time global sea surface temperature analysis. *J. Climate,* **6,** 114-119.

Sherwood, S. C., 1999: Convective precursors and predictability in the tropical western Pacific. *Mon. Wea. Rev.,* **127,** 2977-2991.

Slingo, J. M., et al. 1996: Intraseasonal oscillations in 15 atmospheric general circulation models: Results from an AMIP diagnostic subproject. *Climate Dynamics,* **12**, 325-357.

Sobel, A. H., J. Nilsson, and L. M. Polvani, 2001: The weak temperature gradient approximation and balanced tropical moisture waves. *J. Atmos. Sci.,* **58,** 3650-3665.

Sobel, A. H., and C. S. Bretherton, 2000: Modeling tropical precipitation in a single column. *J. Climate,* **13,** 4378-4392.

Sobel, A. H., and J. D. Neelin, 2006: The boundary layer contribution to intertropical convergence zones in the quasi-equilibrium tropical circulation model framework. *Theor. Comput. Fluid Dyn.,* DOI 10.1007/s00162-006-0033-y.

Su, H., and J. D. Neelin, 2002: Teleconnection mechanisms for tropical Pacific descent anomalies during El Niño. *J. Atmos. Sci.,* **59,** 2694-2712.

Tompkins, A. M., 2001: Organization of tropical convection in low vertical wind shears: The role of water vapor. *J. Atmos. Sci.,* **58,** 529-545.

Zhang, C., M. McGauley, and N. A. Bond, 2004: Shallow meridional circulation in the tropical eastern Pacific. *J. Climate,* **17,** 133-139.

Zhang, C., 2005: Madden-Julian oscillation. *Rev. Geophys.*, **43**, doi: 0.1029/2004RG000158.

Zhang, G. J. and N. A. McFarlane, 1995: Sensitivity of climate simulations to the parameterization of cumulus convection in the Canadian Climate Centre general circulation model. *Atmosphere-Ocean*, **33**, 407-446.

Zhu, H., H. Hendon, and C. Jacob, 2008: Diagnosing MJO and convection behaviour in SP-CAM and CAM simulation. In preparation.

Table and figure captions

Tables

1. Typical values of parameters used in the cumulus parameterization.

Figures

1. Dispersion relation for moisture modes in Raymond-Fuchs theory showing cases with the GMS equal to 0 (solid line), -0.07 (long dash), -0.14 (medium dash), and -0.21 (short dash). (a) Phase speed and (b) growth rate, both as a function of zonal wavenumber assuming a 40000 km zonal domain. Moisture modes with positive GMS are stable.

2. As in figure 1 except dispersion relation for convectively coupled gravity waves. NGMS ranges from -0.21 to $+0.21$. As may be seen the growth rate and phase speed are almost completely unaffected by NGMS – negative NGMS results in a slight decrease in growth rate.

3. Equilibrium precipitation rate and saturation fraction for the cloud resolving model (CRM), the current version of the cumulus parameterization, and the Raymond (2007) version.

4. Plots at 2500 ks of precipitation rate (thick contour 5 mm d^{-1}; thin contours $25, 50, 75, \ldots$ mm d^{-1}), saturation fraction (shading), and surface wind (arrows) for the doubly periodic cases with uniform SST.

5. SST (shading and thin contours, interval 2° C) and intraseasonal rainfall variance (heavy contours, interval 2 mm^2 d^{-2}) for perpetual February conditions (upper panel) and perpetual August conditions (lower panel).

6. Hovmöller diagram for toy model perpetual February simulation showing the surface zonal wind (contours) and precipitation (shading) averaged from the equator south 1500 km. The contour interval for zonal wind is 3 m s^{-1} with solid contours positive, dashed contours negative, and a thick zero contour.

7. As in figure 6 except perpetual August with averaging done from the equator north 1500 km. The dashed lines show the longitude range and time of two snapshots.

8. Snapshots of rainfall rate (gray scale), saturation fraction (contour interval 0.1, heavy contour corresponds to 0.8, negative contours < 0.8), and surface wind (arrow spacing equals 16 m s^{-1}) for the Indo-Pacific warm pool. (a) 14000 ks and (b) 16000 ks, as indicated in figure 7.

9. Plot of the horizontal (pluses) and vertical (bullets) advection parts of the entropy divergence vs. the moisture convergence averaged over the August Indo-Pacific warm pool. All variables have been converted to energy flux units and each point represents a snapshot in time.

10. FNL-derived moisture convergence in energy units (contour interval 100 W m^{-2}, heavy contour zero, darker shading indicates larger values) averaged over $0° − 15°$ N for June-September 2005.

11. Outgoing longwave radiation (contour interval 20 W m^{-2}, thick contour 260 W m^{-2}, darker shades correspond to smaller values) averaged over $0° − 15°$ N for June-September 2005.

12. As in figure 9 except for the FNL.

Parameter	Value	Meaning
λ_c	0.01 ks^{-1}	convective mixing
λ_p	6×10^{-4} ks^{-1}	convective precipitation
λ_s	0.1 ks^{-1}	stratiform precipitation
Γ_t, Γ_s	2 K km^{-1}(both)	lower bound of $d\theta_e/dz$ for strat precip
λ_e	100 ks^{-1}	evaporation of rain
s	6 (dimensionless)	convective rain production stiffness
z_p	6 km	scale height of convective rain
w_t	5 m s^{-1}	precipitation terminal velocity
b	1.5 km	depth of PBL
$\Delta\theta_e$	4 K	slop in convective throttle
ΔT	0.5 K	slop in surface flux throttle
C_D	0.001 (dimensionless)	surface drag coefficient
W	3 m s^{-1}	minimum wind for surface fluxes

Table 1: Typical values of parameters used in the cumulus parameterization.

Figures and tables
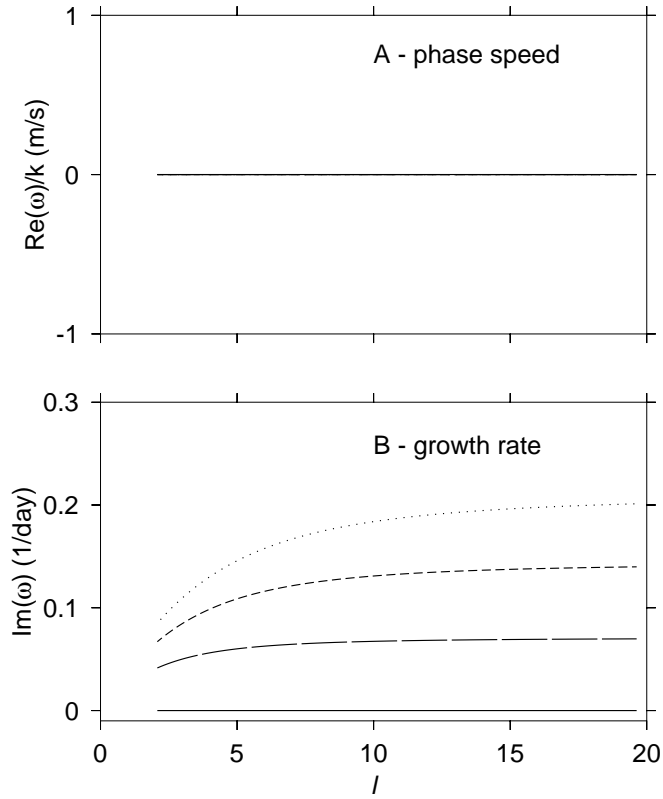
Figure 1: Dispersion relation for moisture modes in Raymond-Fuchs theory showing cases with the GMS equal to 0 (solid line), -0.07 (long dash), -0.14 (medium dash), and -0.21 (short dash). (a) Phase speed and (b) growth rate, both as a function of zonal wavenumber assuming a 40000 km zonal domain. Moisture modes with positive GMS are stable.
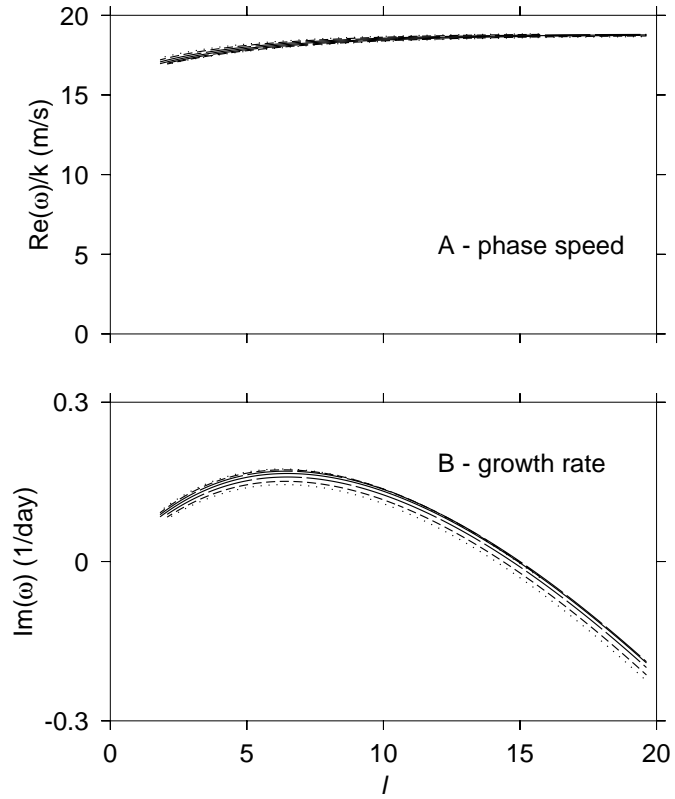
Figure 2: As in figure 1 except dispersion relation for convectively coupled gravity waves. NGMS ranges from −0.21 to +0.21. As may be seen the growth rate and phase speed are almost completely unaffected by NGMS – negative NGMS results in a slight decrease in growth rate.
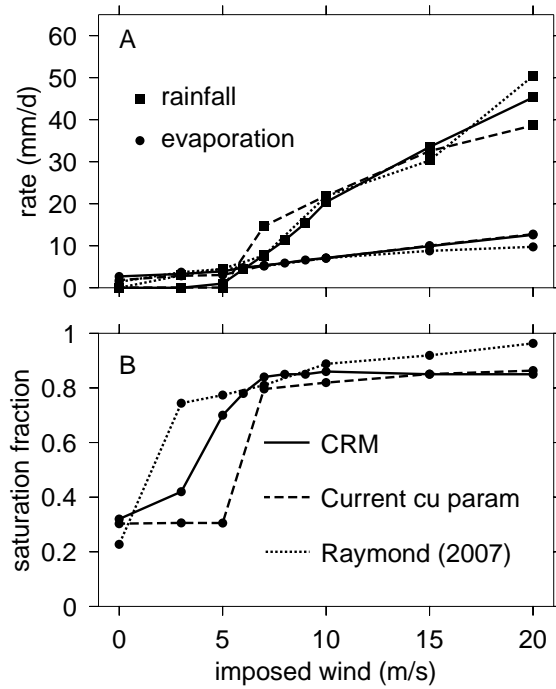
Figure 3: Equilibrium precipitation rate and saturation fraction for the cloud resolving model (CRM), the current version of the cumulus parameterization, and the Raymond (2007) version.
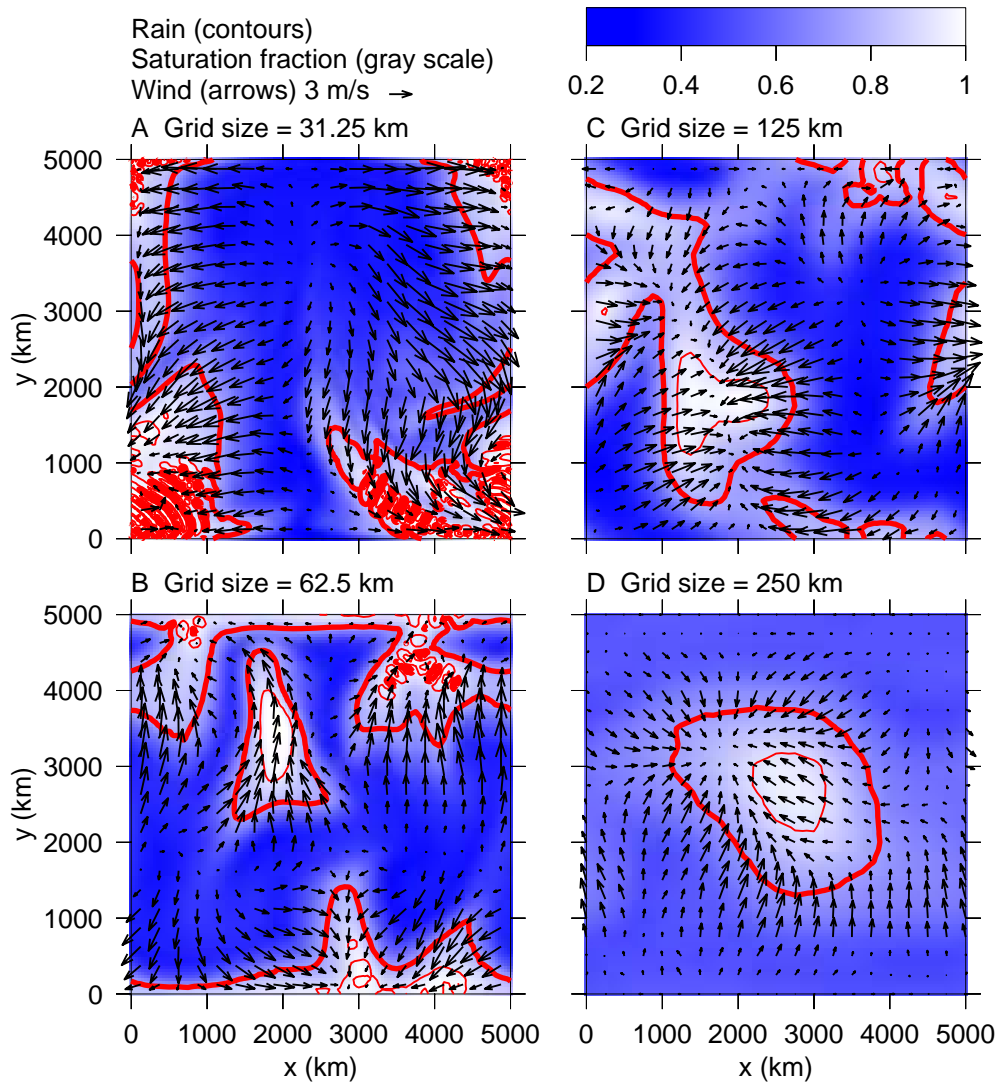
Figure 4: Plots at 2500 ks of precipitation rate (thick contour 5 mm d^{-1}; thin contours 25, 50, 75, ... mm d^{-1}), saturation fraction (shading), and surface wind (arrows) for the doubly periodic cases with uniform SST.
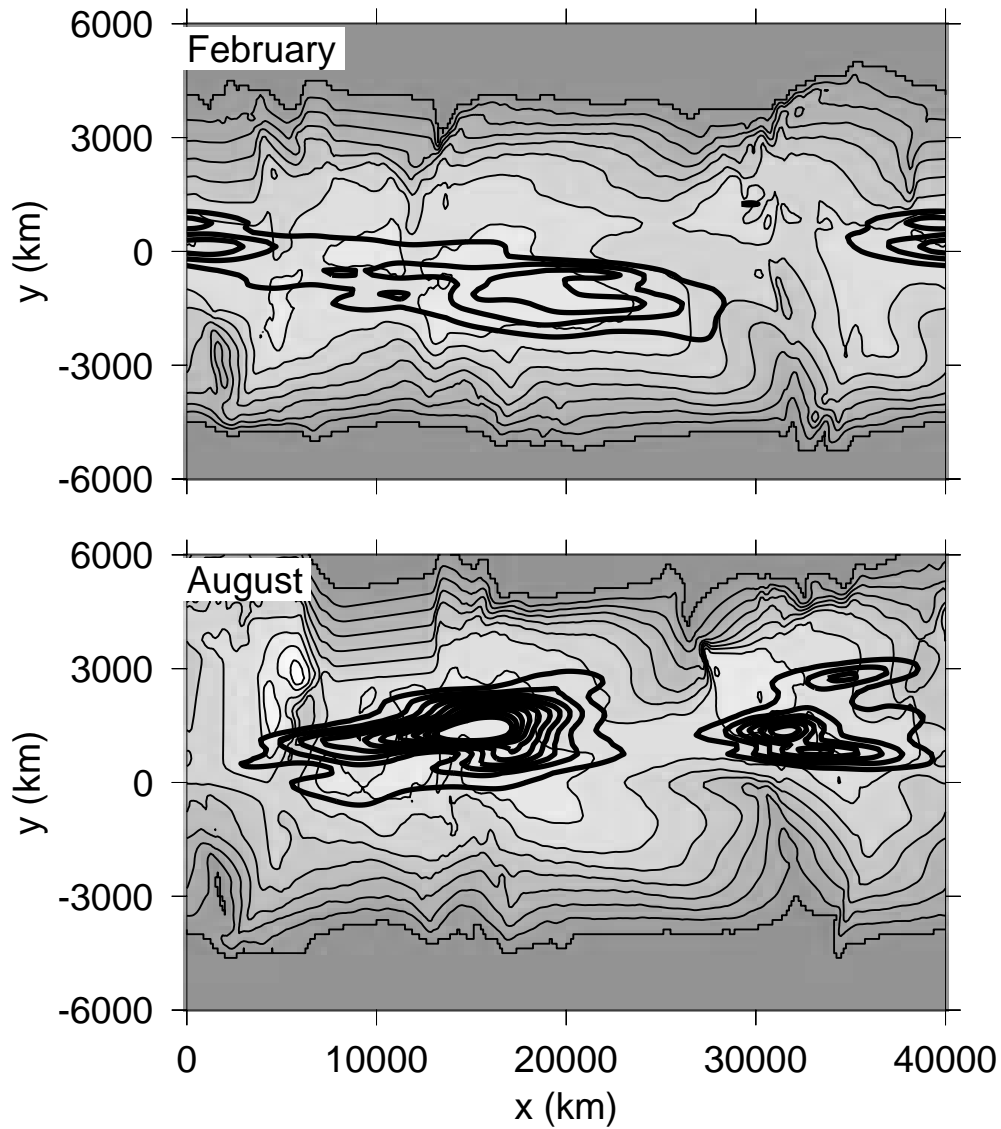
Figure 5: SST (shading and thin contours, interval 2° C) and intraseasonal rainfall variance (heavy contours, interval 2 mm^2 d^{-2}) for perpetual February conditions (upper panel) and perpetual August conditions (lower panel).
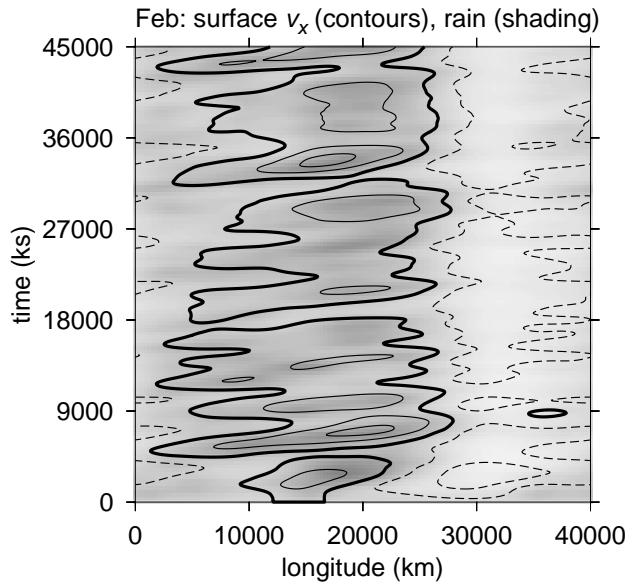
Figure 6: Hovmöller diagram for toy model perpetual February simulation showing the surface zonal wind (contours) and precipitation (shading) averaged from the equator south 1500 km. The contour interval for zonal wind is 3 m s^{-1} with solid contours positive, dashed contours negative, and a thick zero contour.
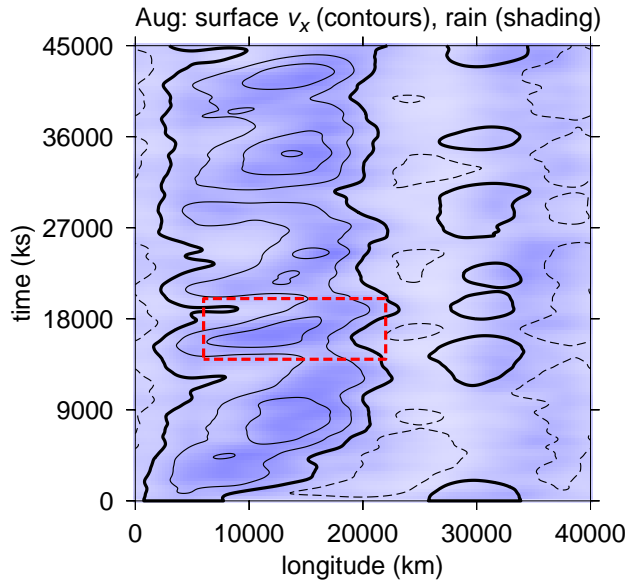
Figure 7: As in figure 6 except perpetual August with averaging done from the equator north 1500 km. The dashed lines show the longitude range and time of two snapshots.
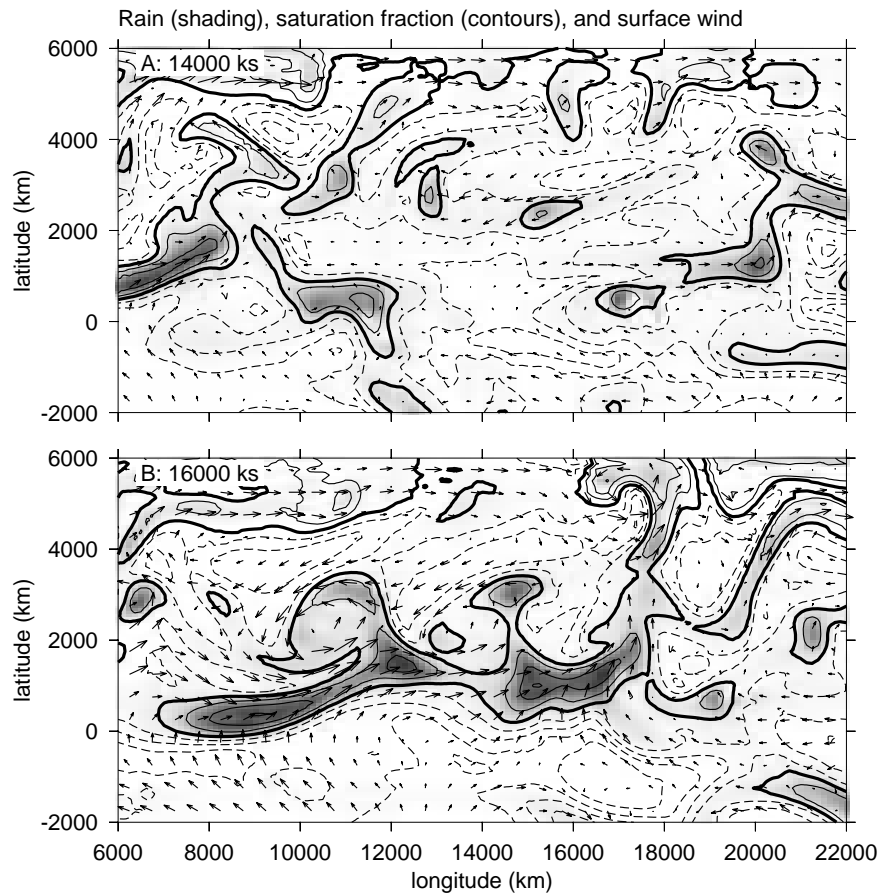
Figure 8: Snapshots of rainfall rate (gray scale), saturation fraction (contour interval 0.1, heavy contour corresponds to 0.8, negative contours < 0.8), and surface wind (arrow spacing equals 16 m s^{-1}) for the Indo-Pacific warm pool. (a) 14000 ks and (b) 16000 ks, as indicated in figure 7.
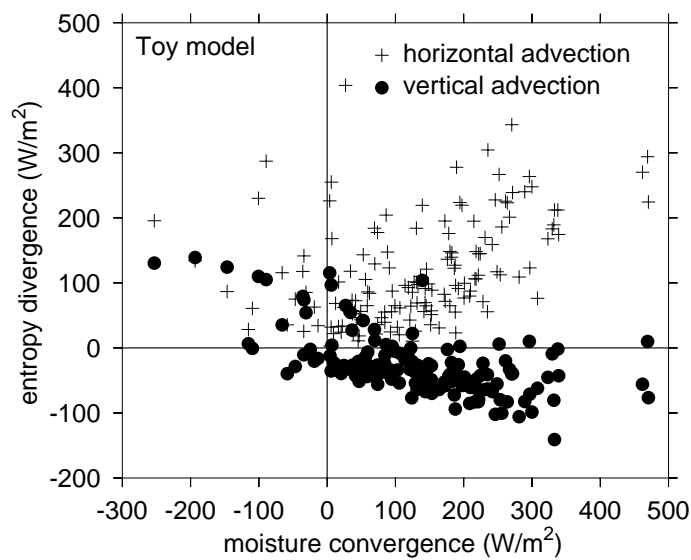
Figure 9: Plot of the horizontal (pluses) and vertical (bullets) advection parts of the entropy divergence vs. the moisture convergence averaged over the August Indo-Pacific warm pool. All variables have been converted to energy flux units and each point represents a snapshot in time.
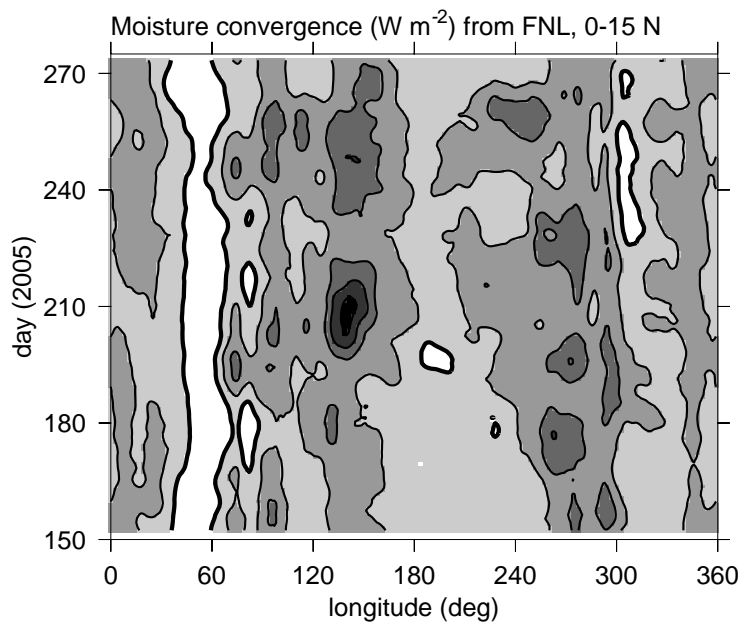

Figure 10: FNL-derived moisture convergence in energy units (contour interval 100 W m^{-2}, heavy contour zero, darker shading indicates larger values) averaged over $0° - 15°$ N for June-September 2005.
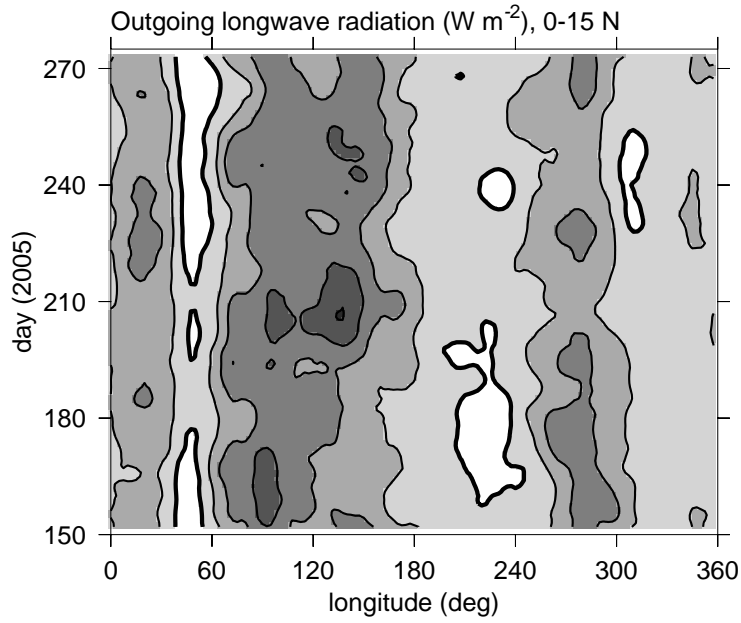
Figure 11: Outgoing longwave radiation (contour interval 20 W m^{-2}, thick contour 260 W m^{-2}, darker shades correspond to smaller values) averaged over $0° - 15°$ N for June-September 2005.
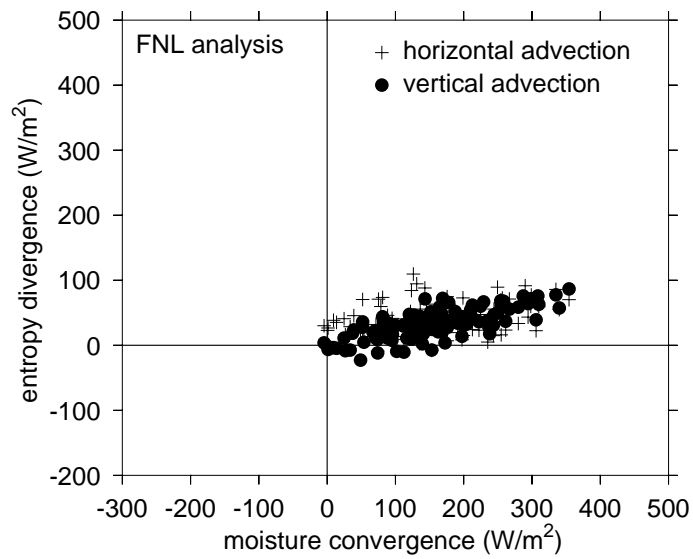

Figure 12: As in figure 9 except for the FNL.